686 *Biochemistry* **2011,** *50,* 686–692
DOI: 10.1021/bi1009425

BIOCHEMISTRY
including biophysical chemistry & molecular biology
Article

A Novel Photosynthetic Strategy for Adaptation to Low-Iron Aquatic Environments[†]

Devendra Chauhan,[‡] I. Mihaela Folea,[§] Craig C. Jolley,*[,‡,▽] Roman Kouřil,[§] Carolyn E. Lubner,[⊥] Su Lin,[‡] Dorota Kolber,[@] Felisa Wolfe-Simon,*[,‡,#,○] John H. Golbeck,[⊥,∥] Egbert J. Boekema,[§] and Petra Fromme*[,‡]

[‡]*Department of Chemistry and Biochemistry, Arizona State University, Tempe, Arizona 85287, United States,* [§]*Groningen Biomolecular Sciences and Biotechnology Institute, University of Groningen, Groningen, The Netherlands,* [∥]*Department of Biochemistry and Molecular Biology, and* [⊥]*Department of Chemistry, Pennsylvania State University, University Park, Pennsylvania 16802, United States,* [@]*Monterey Bay Aquarium Research Institute, Moss Landing, California 95039, United States, and* [#]*Department of Earth and Planetary Sciences, Harvard University, Cambridge, Massachusetts 02138, United States* [▽]*Current address: Department of Chemistry and Biochemistry, Montana State University, Bozeman, MT 59715.* [○]*Current address: U.S. Geological Survey, Menlo Park, CA 94025.*

Received June 11, 2010; Revised Manuscript Received October 8, 2010

ABSTRACT: Iron (Fe) availability is a major limiting factor for primary production in aquatic environments. Cyanobacteria respond to Fe deficiency by derepressing the *isiAB* operon, which encodes the antenna protein IsiA and flavodoxin. At nanomolar Fe concentrations, a PSI−IsiA supercomplex forms, comprising a PSI trimer encircled by two complete IsiA rings. This PSI−IsiA supercomplex is the largest photosynthetic membrane protein complex yet isolated. This study presents a detailed characterization of this complex using transmission electron microscopy and ultrafast fluorescence spectroscopy. Excitation trapping and electron transfer are highly efficient, allowing cyanobacteria to avoid oxidative stress. This mechanism may be a major factor used by cyanobacteria to successfully adapt to modern low-Fe environments.

Mounting evidence shows a striking dependence of photosynthesis on environmental Fe (*1*−*4*). The photosynthetic apparatus is strongly affected by limitations of "free" Fe because the membrane protein complexes that catalyze the light reactions all contain Fe in heme or FeS clusters. Fe limitation is most critical for Photosystem I (PSI),[1] which is the largest sink of Fe as each PSI trimer contains 36 Fe atoms in nine [4Fe-4S] clusters and is further associated with [2Fe-2S] clusters in multiple copies of ferredoxin (*5*).

Cyanobacteria respond to Fe deficiency by lowering the PSI:PSII ratio (*6*) and derepressing the *isiAB* operon (*7*), which encodes the antenna protein IsiA and flavodoxin (IsiB) that functionally replaces the Fe-containing ferredoxin. In 2001, two research groups found that 18 copies of the IsiA protein assemble into a ringlike structure that surrounds the PSI trimer under conditions of short-term Fe starvation (*8*, *9*). In addition, excessive light (*10*), oxidative stress (*11*), high ionic strength (*12*), or heat stress (*13*) induces the expression of the *isiAB* operon. IsiA is functionally versatile; it can serve as an auxiliary antenna system for PSI (*14*, *15*) and has also been shown to play a photoprotective role (*16*) and increase the cyclic electron flow around PSI (*17*). All these functional studies have been performed on isolates from cyanobacteria grown in media without any added Fe, which does not mimic the most prevalent ecologically relevant conditions for cyanobacteria in modern environments (*18*).

Here, we report a unique, potentially evolutionarily significant adaptation of the photosynthetic apparatus in cyanobacteria living under nanomolar Fe conditions.

MATERIALS AND METHODS

Cell Growth and Purification of the PSI−*IsiA$_{DR}$ Supercomplexes*. For standard growth conditions, the cyanobacterium *Thermosynechococcus elongatus* was grown photoautotrophically at 56 °C in a 130 L photobioreactor (Satorius/B. Brown Biotech) in medium D (*19*), under fluorescent cold white light at an irradiance of 100 μmol of photons m^{-2} s^{-1} with a mixture of saturated air and 2% (v/v) CO_2. For growth under Fe deficiency, 12 g of fresh cells was washed three times with 18.2 MΩ cm nanopure water and suspended in a 160 L acid-washed glass container filled with D medium without added Fe at 56 °C. The medium was vigorously agitated with air containing 5% (v/v) CO_2 to ensure a sufficient CO_2 supply as well as homogeneity and equal temperature distribution. The culture was illuminated with tungsten halogen lamps (25 μmol of photons m^{-2} s^{-1}), and the light irradiance was increased to 50 μmol of photons m^{-2} s^{-1} on the 10th day. A daily absorption spectrum was taken to monitor the cell density, the spectral composition, and the formation of PSI−IsiA$_{DR}$ (DR = double ring) supercomplexes. Initially, cells were grown without any additional Fe supplement for 11 days, which led to the consumption of Fe within the cells (in the form of ferritin) as well as in the surroundings (Fe as an impurity). On days 12 and 20, 20 mL of 20 μM $FeCl_3$ was added to the culture. On day 22, the level of illumination was increased to 70 μmol of photons m^{-2} s^{-1}. Cells were harvested after 30 days.

[†]This work was supported by National Science Foundation (NSF) Grant MCB-0417142 to P.F., by a NWO-TOP grant from The Netherlands Organisation for Scientific Research (NWO) to E.J.B., by an NSF Postdoctoral Fellowship in Biology (DBI-0511972) to F.W.-S., and by the U.S. Department of Energy, Basic Energy Sciences, Division of Material Sciences and Engineering, under Contract DE-FG-05-05-ER46222 to J.H.G.

*To whom correspondence should be addressed. P.F.: e-mail, pfromme@asu.edu; phone, (480) 965-9028; fax, (480) 965-2747. C.C. J.: e-mail, jolleycraig@gmail.com; phone, (406) 579-5566; fax, (406) 994-5407. F.W.-S.: e-mail, felisawolfesimon@gmail.com; phone, (650) 329-4426; fax, (650) 329-4463.

[1]Abbreviations: PSI, Photosystem I; Chl, chlorophyll; TEM, transmission electron microscopy; FDAS, fluorescence decay-associated spectra; NADPH, nicotinamide adenine dinucleotide phosphate; SOD, superoxide dismutase.

 Published on Web 10/13/2010

A previously described method was modified for the preparation of thylakoid membranes (*8*, *9*). Cells were washed and resuspended in 10 mM $CaCl_2$, 10 mM $MgCl_2$, 500 mM mannitol, and 20 mM MES buffer (pH 6.5) and passed twice through a chilled cell microfluidizer (Microfluidics) at 12000 psi. Unbroken cells were removed by centrifugation at 4000*g* for 10 min at 4 °C, and thylakoid membranes were harvested from the supernatant. After the chlorophyll *a* concentration had been adjusted to 1.0 mM, membranes were solubilized with 1.5% (w/v) ultrapure *n*-dodecyl β-D-maltoside (β-DDM) (< 0.01% α isomer, from Glycon) at 4 °C for 12 h and then centrifuged at 20000*g* for 20 min to remove insoluble materials. Subsequently, the detergent extract was ultracentrifuged (Beckman Coulter) at 200000*g* and 4 °C for 1 h. The upper dark green portion of the sediment was collected, and the protein complexes were further purified by FPLC/HPLC anion exchange chromatography using a Q-Sepharose column (GE Healthcare). A 25 to 300 mM $MgSO_4$ buffer gradient was used to elute the supercomplexes (Figure S2A of the Supporting Information). The supercomplexes elute in a peak at ~200 mM $MgSO_4$. They were concentrated by ultrafiltration using 100K cutoff ultrafiltration spin filters (Millipore). The samples were further purified by two size exclusion chromatography runs using a Superose-CL6B (GE Healthcare) column (Figure S2B−E of the Supporting Information). Purified PSI−$IsiA_{DR}$ supercomplexes were again concentrated and stored in a buffer solution containing 20 mM MES (pH 6.5), 10 mM $CaCl_2$, 100 mM $MgSO_4$, 0.4 M mannitol, and 0.03% (w/v) β-DDM at −80 °C.

Electron Microscopy and Single-Particle Analysis. Aliquots of purified protein were diluted in a buffer containing 20 mM MES (pH 6.5), 10 mM $CaCl_2$, 100 mM $MgSO_4$, and 0.03% (w/v) β-DDM, applied on carbon-coated glow-discharged grids, and negatively stained with a 2% solution of uranyl acetate. EM was performed on a Philips CM120 electron microscope. Semiautomatic data acquisition was used to record images at a magnification of 80000× with a Gatan 4000 SP 4K slow-scan CCD camera (Gatan, Pleasanton, CA). The pixel size used was 3.75 Å at the specimen level (after the images had been binned). Single-particle analysis was performed with Groningen Image Processing (GRIP). Projections were aligned and subjected to multivariate statistical analysis (MSA). After MSA, particles were classified and summed and class sums were used in a next cycle of multireference alignment, MSA, and classification (*20*−*27*). Resolution was measured using Fourier ring correlation and the 3σ criterion (*28*−*30*). The results of the single-particle analysis shown in Figure 1 represent averages of a homogeneous class of 1024 top-view projections. The truncated version and 2D projection map of the PSI trimer (*5*) at 15 Å resolution [Protein Data Bank (PDB) entry 1JB0] was generated using routines from the EMAN package (*19*). For better visibility of individual PSI subunits, cofactors were omitted in the truncated version of the X-ray structure (Figure 1B).

Dual-Beam Spectrophotometry. The Chl/P_{700} ratio of dissolved PSI crystals and PSI−$IsiA_{DR}$ supercomplexes was determined by measuring the amount of oxidized P_{700}. The proteins were suspended in a buffer containing 20 mM MES (pH 6.4), 100 mM $MgSO_4$, and 0.03% β-DDM. The sample (5 mL) was equally divided between two glass cuvettes (2.5 mL each). Ten microliters of 0.5 M ascorbate was added to one cuvette, and 10 μL of 0.1 M potassium ferricyanide was added to the other. The absorption difference spectrum (reduction − oxidation) was measured between 650 and 850 nm using a Cary dual-beam spectrophotometer. The Chl/P_{700} ratios were calculated using an extinction coefficient of 64000 M^{-1} cm^{-1} for P_{700} (*31*).

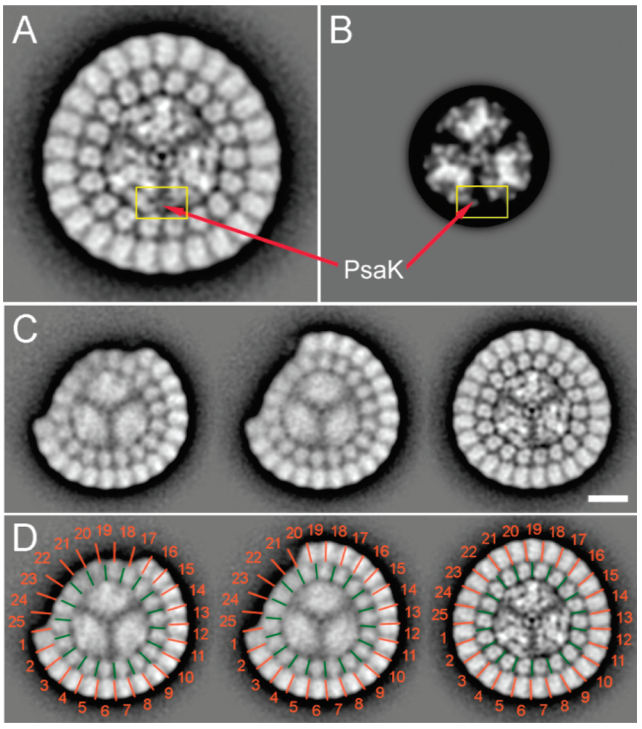

FIGURE 1: Structural comparison between the PSI−IsiA supercomplex and the PSI trimer using results of single-particle TEM and image analysis. (A) Projection map of the PSI−IsiA supercomplex at 15 Å resolution from *T. elongatus* grown at nanomolar Fe levels. The PSI trimer is surrounded by 43 IsiA subunits, with 18 and 25 in the inner and outer rings, respectively. (B) Generated 2D projection map of the PSI trimer from the 2.5 Å X-ray structure (*5*), truncated at 15 Å resolution to allow direct comparison with panel A. The general features of both structures are similar except that the peripheral PsaK subunits show tighter interactions (yellow box) in the supercomplex. (C) PSI−IsiA supercomplexes with incomplete outer rings containing 16 (left), 19 (center), and all 25 (right) IsiA subunits. All 2D projection maps represent top view projections of PSI from the stromal side and are derived from class averaging of the 1024 single-particle projections. The scale bar is 10 nm. (D) Comparison of the location of individual IsiA subunits of the intact ring and the assembly intermediates. The spaces between the IsiA monomers in the fully assembled complex (right) are indicated by green and red bars for the inner and outer rings, respectively. The spacing between the IsiA complexes is slightly larger in the partially assembled complexes, which can be seen near the top of the images.

Picosecond Fluorescence Spectroscopy. Fluorescence decay kinetics were measured using the time-correlated single-photon counting (TCSPC) technique. The excitation source was a titanium sapphire (Ti:S) laser (Spectra-Physics, Millennia pumped Tsunami) with a 130 fs pulse duration operated at 80 MHz. The laser output was sent through a frequency doubler and pulse selector (Spectra Physics, model 3980) to produce 400 nm excitations at 4 MHz. The excitation beam was attenuated as needed to produce 1000−5000 fluorescence counts per second. Fluorescence emission was collected at a right angle to the excitation beam and detected using a double-grating monochromator (Jobin-Yvon, Gemini-180) and a microchannel plate photomultiplier tube (Hamamatsu R3809U-50). Fluorescence decay curves were collected over the wavelength region from 660 to 770 nm at 10 nm intervals. Data acquisition was conducted using a single-photon counting card (Becker-Hickl, SPC-830) on a 3.3 ns time scale. The instrument response function (IRF) had a full width at half-maximum (fwhm) of ~34 ps, as verified by scattering from a nondairy coffee creamer solution.

Table 1: Ratio of Chlorophyll to P_{700} in the PSI−IsiA Supercomplexes[a]

sample	abbreviation	Chl/supercomplex	Chl/P_{700}	IsiA/PSI (from Chl/P_{700})	IsiA/PSI (from TEM)
PSI with complete double ring	PSI−$IsiA_{DR}$	855 ± 15	285 ± 5	43 ± 1	43
PSI with partial double ring	PSI−$IsiA_{PDR}$	675 ± 75	225 ± 25	30 ± 6	24−37
PSI with single ring	PSI−$IsiA_{SR}$	573 ± 30	191 ± 10	21 ± 3	18
PSI trimer	PSI	285 ± 3	95 ± 1	0	0

[a]Determination of Chl *a*/P_{700} ratios of various purified PSI−IsiA supercomplexes by dual-beam UV−vis spectroscopy. Dissolved PSI crystals from *T. elongatus* were used as a control.

Data were analyzed with the home-written software package ASUFIT (www.public.asu.edu/~laserweb/asufit/asufit.html), using a sum of exponential decays for global analysis. The fit quality was judged using χ^2 statistics and weighted residuals; fluorescence decay curves were considered acceptable only if the χ^2 value for each individual wavelength and for the global fit was ≤1.20. To produce the fluorescence decay-associated spectra (FDAS) shown in Figure S6 of the Supporting Information, steady-state fluorescence spectra [$F(\lambda)$] were used to scale the amplitudes [$A_i(\lambda)$] obtained from global fitting by their appropriate lifetimes (τ_i) so that $F(\lambda) = \sum_i \tau_i A_i(\lambda)$. Steady-state fluorescence emission spectra were recorded on a home-built fluorimeter (*32*) consisting of a xenon lamp as the excitation source, excitation and emission monochromators (SpectraPro-150, Acton Research, Dayton, OH), a sample holder, and a CCD array detector (NTE/CCD-1340/100-EMB..FG, Princeton Instruments, Monmouth Junction, NJ).

Ultrafast Fluorescence Spectroscopy. The time versus wavelength fluorescence intensity surfaces were recorded on a system consisting of an ultrafast laser and a streak camera. The 130 fs light pulses at 800 nm were generated by a mode-locked Ti:S laser (Mira 900, Coherent Laser) pumped by a frequency-doubled Nd:YVO_4 laser (44% from an 18 W Verdi, Coherent Laser). The repetition rate of the Ti:S laser was reduced to 4.75 MHz by a pulse picker (model 9200, Coherent Laser). The excitation light (800 nm) was frequency doubled to 400 nm and focused onto a sample cuvette with a 3 mm path length. Fluorescence was collected at a right angle to the excitation beam and focused on the entrance slit of a Chromex 250IS spectrograph that was coupled to a Hamamatsu C5680 streak camera with a M5675 synchroscan sweep unit. The streak images were recorded on a Hamamatsu C4742 CCD camera. Measurements were taken on 800 ps, 1.4 ns, and 2 ns time scales, with 1024 pixels of time resolution. The fwhm of the overall time response of this system was ~6 ps at the 800 ps time scale, ~12 ps at the 1.4 ns time scale, and ~20 ps at the 2 ns time scale. The spectral resolution was 0.124 nm in the spectral range of 650−777 nm (1024 pixels). To eliminate the possibility of excitation disappearance due to singlet−singlet annihilation, we also measured fluorescence decay in the PSI−$IsiA_{DR}$ supercomplex after decreasing the excitation power to ~3 pJ/pulse; global analysis gave essentially the same lifetimes and spectral shapes (see Figure S7 of the Supporting Information), indicating that the contribution of singlet−singlet annihilation to the fluorescence decay measurements at full intensity (~30 pJ/pulse) was negligible. Global analysis was performed using ASUFIT. The 1024 kinetic traces were binned, resulting in a spectral resolution of 4.95 nm. A Gaussian-shaped instrument response function was used in the fitting.

RESULTS AND DISCUSSION

T. elongatus was cultured at 2.5 nM Fe and harvested after 30 days. PSI−IsiA supercomplexes were solubilized from the membrane in the form of a protein−detergent micelle in β-DDM and purified by a combination of differential centrifugation, ion exchange chromatography, and size exclusion chromatography (see Materials and Methods for more details on the isolation procedure). The PSI−IsiA supercomplexes are very abundant in the cells, and ~80% of all chlorophylls in the membrane can be isolated in the form of PSI−IsiA supercomplexes.

The isolated supercomplexes are remarkably stable. The different PSI−IsiA supercomplexes can be repurified multiple times using gel filtration chromatography without any measurable change in size or cofactor composition. Strong cofactor binding is also indicated by the extremely small amount of long-lived fluorescence (decay constant of > 1 ns) observed in the streak camera data sets (see below). The long-lived fluorescence remains low even after storage for one week at 4 °C. The supercomplexes even survive harsher detergent treatment and do not disassemble in the presence of high concentrations of short chain detergents such as 2% octyl glycoside. The supercomplexes are fully stable in this detergent, while the PSI trimer without IsiA is disassembled into monomers upon treatment with octyl glycoside. These indications of stability suggest that the partially assembled supercomplexes (Figure 1C) might be in vivo assembly intermediates and not larger supercomplexes in the process of detergent-induced disassembly.

The Chl/P_{700} ratio of the supercomplexes was determined by dual-beam spectrophotometry. Three types of PSI supercomplexes were isolated, each with a unique Chl/P_{700} ratio (see Table 1). The largest supercomplex contained 285 ± 5 Chl molecules/PSI monomer (855 Chl molecules/trimer), a size increase of 296% relative to the PSI trimer, which binds 96 Chl molecules/monomer (*5*).

To gain insight into the effects of antenna size on the light harvesting efficiency and the kinetics of energy migration, fluorescence decay from the various PSI−IsiA supercomplexes was measured using an ultrafast streak camera setup. Fluorescence decay-associated spectra (FDAS) were calculated from these data (Figure 2). The spectral shape of the fastest component (7−10 ps) strikingly changed with increased antenna size. In the PSI trimer, this component is nearly conservative, with the positive peak (indicating a fluorescence decay) and a negative peak (indicating an increase in fluorescence) being nearly equal in size. This indicated efficient downhill energy transfer (*14*, *15*, *33*) from the "blue" bulk population of chlorophylls to the red-shifted chlorophylls. The equal positive and negative amplitudes suggested that no trapping (i.e., use of excitation energy for catalysis of charge separation) takes place on this time scale. The 36 ps component (*34*−*38*) in the PSI trimer and its peak at ~720 nm suggest a trapping process that is limited by escape from red-shifted chlorophyll sites, while a shoulder at ~690 nm indicates trapping from bulk sites.

Two major changes took place as the antenna size was increased by the additional IsiA proteins. First, the fast component loses its conservative character, with the amplitude of the negative red peak decreasing, while that of the positive peak

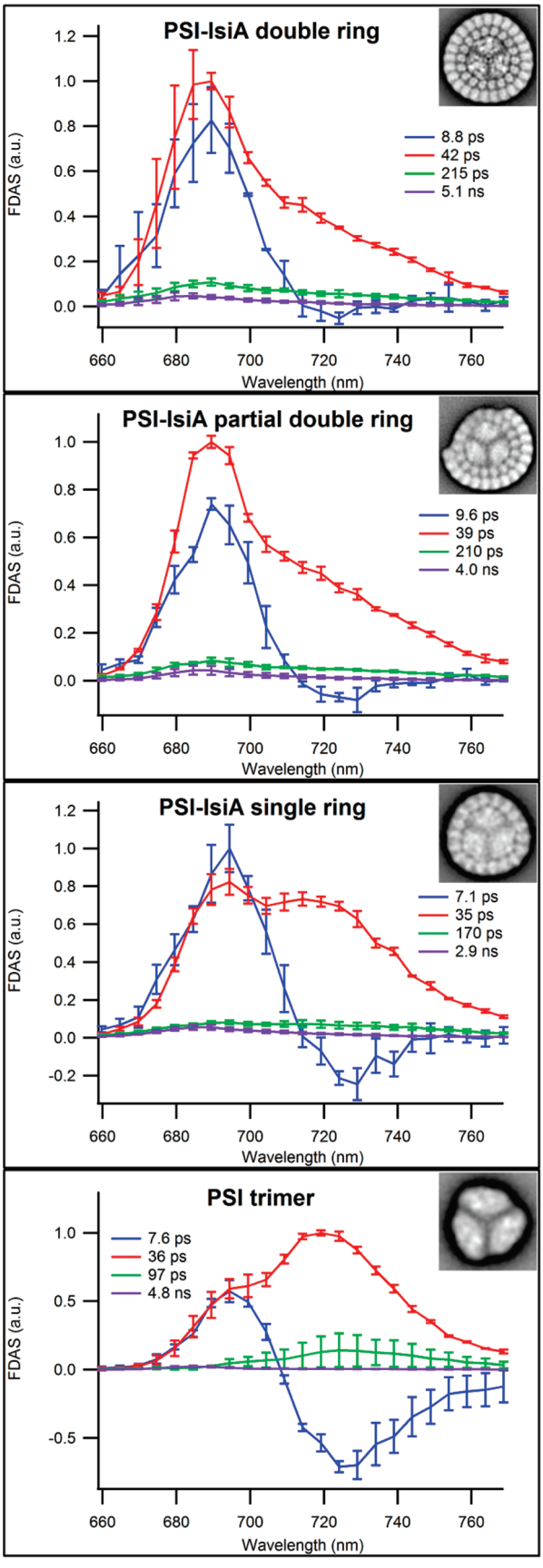

FIGURE 2: Fluorescence decay-associated spectra (FDAS) determined by global analysis of streak camera data. Curves are averages from data sets collected at different time scales. The lifetimes and spectral shapes obtained with streak camera measurements were confirmed by time-correlated single-photon counting (Figures S6 and S7 of the Supporting Information).

increases. This indicated that, in contrast to the PSI trimer, significant trapping takes place on this time scale in the PSI−IsiA supercomplexes. The red-shifted pigments played a diminished role with increasing antenna size because of the blue shift of the chlorophylls in IsiA relative to PSI; the excitons are less likely to become temporarily trapped by the red-shifted chlorophylls (associated only with PSI) before migrating to P_{700}. A further possibility is that one of the major red-shifted chlorophyll sites is located on the periphery of the PSI trimer (*39*), and its strong excitonic coupling may be disrupted by IsiA binding, thereby decreasing its red shift.

The exciton trapping time increases only slightly, from 36 ps for the PSI trimer to 42 ps for the PSI−$IsiA_{DR}$ supercomplex. Although the overall size of the antenna complex has tripled, the average exciton trapping time has increased by a mere 16%, indicating efficient migration of energy to P_{700}. The absence of any high-amplitude components on the >50 ps time scale indicates that the PSI−$IsiA_{DR}$ supercomplexes are energetically well-coupled, and that even the largest PSI−IsiA supercomplexes form an extremely well-integrated pigment network.

Size exclusion chromatography fractions of PSI−IsiA supercomplexes were analyzed by electron microscopy and single-particle image analysis. In total, we recorded 1500 images of negatively stained specimens and analyzed 70000 single-particle projections (Figure 1). Each 2D projection map shown in Figure 1 represents an average of a homogeneous class of 1024 top view projections. The largest circular particle was resolved at 15 Å resolution and was identified as a PSI trimer containing a double ring of IsiA proteins (Figure 1A). The inner ring contained 18 IsiA subunits, and the outer ring contained 25 copies (Figure 1A). This PSI−$IsiA_{DR}$ supercomplex is the largest membrane-bound photosynthetic structure that has been characterized to date.

All stromal subunits are present, including PsaC, which contains terminal FeS clusters F_A and F_B. The 2D electron density map (Figure 1A) shows the stromal hump of PSI, which is identical in shape to the hump in the PSI trimer (Figure 1B), thereby clearly indicating the presence of all three subunits. Further strong support is provided by the spectroscopic data for the kinetics of P_{700}^+ re-reduction (Figure S5 of the Supporting Information); the similarity between PSI and the PSI−$IsiA_{DR}$ supercomplex suggests that the acceptor side of PSI is intact in the supercomplex. Although PsaE and PsaD contain no cofactors, they are necessary for the binding of PsaC in a stable functional form to the PSI core. We have further confirmed the presence of the extrinsic subunits by SDS−PAGE (Figure S3 of the Supporting Information) and analyzed the PsaC content of the supercomplex by Western blot analysis (Figure S4 of the Supporting Information) and by non-heme Fe assays and acid-labile sulfide assays; these experiments are described in detail in the Supporting Information.

Figure 1C shows assembly intermediates of the PSI−$IsiA_{DR}$ supercomplex that contain either 16 or 19 copies of IsiA in the outer ring. Empty IsiA rings (without a central PSI trimer) were not observed. The configuration of the outer ring in the PSI−$IsiA_{DR}$ supercomplex demonstrates an astonishing symmetry mismatch with the C_3 symmetry of the PSI trimer and the inner IsiA ring (see Figure 1D). The intrinsic flexibility of the IsiA subunits allows them to pack more closely in the final, assembled supercomplex than in the partial rings. The positions of the IsiA subunits in the inner ring are also not identical in the three supercomplexes; those without outer ring neighbors show a looser packing.

This variability in the association of PSI with IsiA has been observed in several previous studies. The initial structures of the PSI complex surrounded by 18 IsiA proteins (*8*, *9*) and a resulting 3D model (*40*) led researchers to believe that six IsiA monomers would bind strongly to a single PSI monomer, preserving the C_3 symmetry. It was suggested that the organization of the IsiA and PSI chlorophylls is optimized for the efficient transfer of energy across this optimized interface, for instance, by the three chlorophylls bound to the PsaJ protein and possibly by hitherto unrecognized linker chlorophylls (*41*, *42*). Later, the role of PsaF and PsaJ in the binding of IsiA to the PSI core trimer was investigated in a PsaF/PsaJ double mutant of *Synechocystis* sp. PCC 6803 (*43*). PSI−IsiA single-ring supercomplexes can still be formed, but the IsiA ring consists in this mutant of 17 units, breaking the symmetry observed in PSI−IsiA supercomplexes from wild-type cells. The size of the IsiA ring around the photosystem is strongly determined by the circumference of the PSI trimer, in addition to specific PSI−IsiA interaction sites. This indicates that PsaF and PsaJ are not essential for the binding of IsiA to PSI. An analysis of *Synechocystis* PCC 6803 cells grown for varying amounts of time in Fe-free media (conditions that induce severe chlorosis) demonstrated that several types of PSI−IsiA supercomplexes, along with various associations of IsiA proteins with monomeric PSI and empty rings of IsiA without PSI, can exist (*44*). Analysis of various PSI−IsiA supercomplexes from a *Synechocystis* sp. PCC 6803 mutant lacking the PsaL subunit indicates that PsaL facilitates the formation of IsiA rings around PSI monomers but is not an obligatory structural component in the formation of PSI−IsiA complexes (*45*) (see ref *46* for a recent review, as well as the Supporting Information). All these results suggest that IsiA is sufficiently versatile to associate with PSI in a variety of different configurations, rather than being rigidly optimized for a specific supercomplex geometry.

The implications of a highly efficient PSI−$IsiA_{DR}$ supercomplex for the adaptation of cyanobacteria to Fe deficiency are profound. The addition of 43 IsiA proteins increases the effective antenna size by 296%, with only a modest increase in the exciton trapping time scale, allowing each PSI reaction center to absorb more photons and process more electrons per unit time. This increased throughput means that fewer PSI complexes are required per cell, decreasing cellular Fe requirements.

isiAB may also function in cellular adaptation to other environmental stresses; it is induced under oxidative stress conditions (*11*, *12*, *47*) and in mutants where the transfer of electrons from water to NADPH has been inhibited (*48*, *49*). This could suggest a connection between oxidative stress and Fe deprivation. The oxidative stress response involves investing in Fe-containing antioxidant proteins, including the powerful antioxidants FeSOD and catalase (*50*). *isiAB* expression may help to compensate for this increased Fe demand, allowing the cell to cope with oxidative stress without compromising energy production.

The intensive usage of Fe in oxygenic photosynthesis has been explained as reflecting the high-Fe conditions under which photosynthesis emerged (*51*, *52*). Photosynthesis by early cyanobacteria led to a dramatic increase in the atmospheric level of O_2. This in turn effected a major change in the ocean−atmosphere system, causing a "rusting out" of the oceanic Fe inventory over the past 3 billion years (*53*). Cyanobacteria necessarily had to evolve to cope with this change in the bioavailability of Fe.

Low-Fe conditions (approximately nanomolar) are prevalent in modern freshwater and marine aquatic environments. For example, many marine cyanobacteria contain either an *isiA* gene

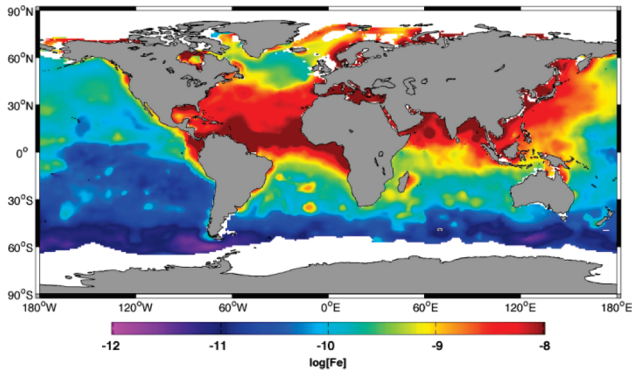

FIGURE 3: Global distribution of Fe in the world's oceans. Cooler colors identify low, subnanomolar Fe levels that generally correlate with regions of low photosynthetic activity (*1*−*3*). Warmer colors indicate higher Fe concentrations, usually found in most of the coastal oceans, in the upwelling regions of the Atlantic Ocean and Eastern Pacific Ocean, and in the areas of high supply of aeolian dust from the Sahara Desert and Gobi Desert, generally corresponding to areas of high photosynthetic activity. This figure is based on data from Gao et al. (*59*) processed according to the method of Berman-Frank et al. (*60*).

(e.g., *Synechococcus*) or a *pcb* gene (e.g., *Prochlorococcus*) (*54*, *55*), which are similar to *isiA* and encode a peripheral antenna protein augmenting both PSI and PSII (*56*). Others, such as the open-ocean diazotroph *Trichodesmium*, which plays a key role in global C and N budgets and has particularly high Fe demands because of its photosynthetic and N_2-fixing capabilities, contain the "classical" *isiAB* gene cluster (*57*). Cyanobacteria living under Fe- or light-limited conditions often contain *isiA*/*pcb* (*54*), whereas some coastal strains have lost these genes (*55*) and are unable to adapt to low-light, low-Fe environments. Given that our data suggest that an IsiA supercomplex could significantly contribute to adaptation under Fe stress in freshwater, cyanobacteria in Fe-limited marine environments may employ a similar strategy. Complete evaluation of this hypothesis will require more genomic information about cyanobacteria from diverse environments and presents an intriguing avenue for future study. More than 50% of the global primary production occurs in the photic zone that generally contains subnanomolar levels of soluble Fe (Figure 3) (*58*), underscoring the significance of Fe stress for aquatic ecology and global climate and the need for photosynthetic organisms to evolve strategies for surviving in Fe-limited environments.

In conclusion, our data point to a novel and potentially evolutionarily important structure that is induced in cyanobacteria grown under ecologically relevant Fe stress conditions. The PSI−$IsiA_{DR}$ supercomplex exhibits an increased optical cross section, allowing the cells to adapt to lower environmental Fe levels. This may represent another example of how changes in the bioavailability of Fe over geologic time have been imprinted on the survival arsenal used by modern cyanobacteria.

ACKNOWLEDGMENT

We thank Dr. W. Keegstra and Dr. G. T. Oostergetel for discussions and help with EM data processing, as well as the anonymous reviewers of the manuscript for their helpful comments.

SUPPORTING INFORMATION AVAILABLE

Figures S1−S9, detailed experimental procedures, and discussion. This material is available free of charge via the Internet at http://pubs.acs.org.

REFERENCES

1. Eldridge, M., Trick, C., Alm, M., DiTullio, G., Rue, E., Bruland, K., Hutchins, D., and Wilhelm, S. (2004) Phytoplankton community response to a manipulation of bioavailable iron in HNLC waters of the subtropical Pacific Ocean. *Aquat. Microb. Ecol. 35*, 79–91.
2. Martin, J., and Fitzwater, S. (1988) Iron deficiency limits phytoplankton growth in the north-east Pacific subarctic. *Nature 331*, 341–343.
3. Wilhelm, S. (1995) Ecology of iron-limited cyanobacteria: A review of physiological responses and implications for aquatic systems. *Aquat. Microb. Ecol. 9*, 295–303.
4. Webb, E. A., Moffett, J. W., and Waterbury, J. B. (2001) Iron stress in open-ocean cyanobacteria (*Synechococcus*, *Trichodesmium*, and *Crocosphaera* spp.): Identification of the IdiA protein. *Appl. Environ. Microbiol. 67*, 5444–5452.
5. Jordan, P., Fromme, P., Witt, H. T., Klukas, O., Saenger, W., and Krauss, N. (2001) Three-dimensional structure of cyanobacterial photosystem I at 2.5 Å resolution. *Nature 411*, 909–917.
6. Guikema, J. A., and Sherman, L. A. (1983) Organization and function of chlorophyll in membranes of cyanobacteria during iron starvation. *Plant Physiol. 73*, 250–256.
7. Duehring, U., Axmann, I. M., Hess, W. R., and Wilde, A. (2006) An internal antisense RNA regulates expression of the photosynthesis gene isiA. *Proc. Natl. Acad. Sci. U.S.A. 103*, 7054–7058.
8. Bibby, T. S., Nield, J., and Barber, J. (2001) Iron deficiency induces the formation of an antenna ring around trimeric photosystem I in cyanobacteria. *Nature 412*, 743–745.
9. Boekema, E. J., Hifney, A., Yakushevska, A. E., Piotrowski, M., Keegstra, W., Berry, S., Michel, K. P., Pistorius, E. K., and Kruip, J. (2001) A giant chlorophyll-protein complex induced by iron deficiency in cyanobacteria. *Nature 412*, 745–748.
10. Havaux, M., Guedeney, G., Hagemann, M., Yeremenko, N., Matthijs, H. C. P., and Jeanjean, R. (2005) The chlorophyll-binding protein IsiA is inducible by high light and protects the cyanobacterium *Synechocystis* PCC6803 from photooxidative stress. *FEBS Lett. 579*, 2289–2293.
11. Yousef, N., Pistorius, E. K., and Michel, K. P. (2003) Comparative analysis of idiA and isiA transcription under iron starvation and oxidative stress in *Synechococcus elongatus* PCC 7942 wild-type and selected mutants. *Arch. Microbiol. 180*, 471–483.
12. Vinnemeier, J., Kunert, A., and Hagemann, M. (1998) Transcriptional analysis of the isiAB operon in salt-stressed cells of the cyanobacterium *Synechocystis* sp. PCC 6803. *FEMS Microbiol. Lett. 169*, 323–330.
13. Kojima, K., Suzuki-Maenaka, T., Kikuchi, T., and Nakamoto, H. (2006) Roles of the cyanobacterial isiABC operon in protection from oxidative and heat stresses. *Physiol. Plant. 128*, 507–519.
14. Andrizhiyevskaya, E. G., Frolov, D., van Grondelle, R., and Dekker, J. P. (2004) Energy transfer and trapping in the Photosystem I complex of *Synechococcus* PCC 7942 and in its supercomplex with IsiA. *Biochim. Biophys. Acta 1656*, 104–113.
15. Melkozernov, A. N., Bibby, T. S., Lin, S., Barber, J., and Blankenship, R. E. (2003) Time-resolved absorption and emission show that the CP43′ antenna ring of iron-stressed *Synechocystis* sp. PCC6803 is efficiently coupled to the photosystem I reaction center core. *Biochemistry 42*, 3893–3903.
16. Sandstrom, S., Park, Y. I., Oquist, G., and Gustafsson, P. (2001) CP43′, the isiA gene product, functions as an excitation energy dissipator in the cyanobacterium *Synechococcus* sp. PCC 7942. *Photochem. Photobiol. 74*, 431–437.
17. Ivanov, A. G., Park, Y. I., Miskiewicz, E., Raven, J. A., Huner, N. P., and Oquist, G. (2000) Iron stress restricts photosynthetic intersystem electron transport in *Synechococcus* sp. PCC 7942. *FEBS Lett. 485*, 173–177.
18. Duce, R. A., and Tindale, N. W. (1991) Atmospheric transport of iron and its deposition in the ocean. *Limnol. Oceanogr. 36*, 1715–1726.
19. Rippka, R. (1988) Isolation and purification of cyanobacteria. *Methods Enzymol. 167*, 3–27.
20. van Heel, M., and Frank, J. (1981) Use of multivariate statistics in analyzing the images of biological macromolecules. *Ultramicroscopy 6*, 187–194.
21. van Heel, M., and Stöffler-Meilicke, M. (1985) Characteristic Views of *E. coli* and *B. stearothermophilus* 30S Ribosomal Subunits in the Electron Microscope. *EMBO J. 4*, 2389–2395.
22. van Heel, M. (1989) Classification of very large electron microscopical image data sets. *Optik 82*, 114–126.
23. Borland, L., and van Heel, M. (1990) Classification of image data in conjugate representation spaces. *J. Opt. Soc. Am. A 7*, 601–610.
24. Penczek, P., Radermacher, M., and Frank, J. (1992) Three-dimensional reconstruction of single particles embedded in ice. *Ultramicroscopy 40*, 33–53.
25. van Heel, M., Gowen, B., Matadeen, R., Orlova, E. V., Finn, R., Pape, T., Cohen, D., Stark, H., Schmidt, R., Schatz, M., and Patwardhan, A. (2000) Single-particle electron cryo-microscopy: Towards atomic resolution. *Q. Rev. Biophys. 33*, 307–369.
26. Frank, J. (2002) Single-particle imaging of macromolecules by cryo-electron microscopy. *Annu. Rev. Biophys. Biomol. Struct. 31*, 303–319.
27. Frank, J. (2006) Three-dimensional electron microscopy of macromolecular assemblies: Visualization of biological molecules in their native state, 2nd ed., Oxford University Press, Oxford, U.K.
28. Saxton, W. O., and Baumeister, W. (1982) The correlation averaging of a regularly arranged bacterial cell envelope protein. *J. Microsc. (Oxford, U.K.) 127*, 127–138.
29. van Heel, M. (1982) Detection of objects in quantum-noise-limited images. *Ultramicroscopy 7*, 331–341.
30. van Heel, M. (1987) Similarity measures between images. *Ultramicroscopy 21*, 95–99.
31. Kitmitto, A., Holzenburg, A., and Ford, R. C. (1997) Two-dimensional crystals of photosystem I in higher plant grana margins. *J. Biol. Chem. 272*, 19497–19501.
32. Kelbauskas, L., Chan, N., Bash, R., Yodh, J., Woodbury, N., and Lohr, D. (2007) Sequence-dependent nucleosome structure and stability variations detected by Förster resonance energy transfer. *Biochemistry 46*, 2239–2248.
33. Du, M., Xie, X. L., Jia, Y. W., Mets, L., and Fleming, G. R. (1993) Direct observation of ultrafast energy transfer in PSI core antenna. *Chem. Phys. Lett. 201*, 535–542.
34. Gobets, B., and van Grondelle, R. (2001) Energy transfer and trapping in photosystem I. *Biochim. Biophys. Acta 1507*, 80–99.
35. Hastings, G., Hoshina, S., Webber, A. N., and Blankenship, R. E. (1995) Universality of energy and electron transfer processes in photosystem I. *Biochemistry 34*, 15512–15522.
36. Holzwarth, A. R., Schatz, G., Brock, H., and Bittersmann, E. (1993) Energy transfer and charge separation kinetics in photosystem I: Part 1: Picosecond transient absorption and fluorescence study of cyanobacterial photosystem I particles. *Biophys. J. 64*, 1813–1826.
37. Gobets, B., van Stokkum, I. H., Rogner, M., Kruip, J., Schlodder, E., Karapetyan, N. V., Dekker, J. P., and van Grondelle, R. (2001) Time-resolved fluorescence emission measurements of photosystem I particles of various cyanobacteria: A unified compartmental model. *Biophys. J. 81*, 407–424.
38. Byrdin, M., Rimke, I., Schlodder, E., Stehlik, D., and Roelofs, T. A. (2000) Decay kinetics and quantum yields of fluorescence in photosystem I from *Synechococcus elongatus* with P700 in the reduced and oxidized state: Are the kinetics of excited state decay trap-limited or transfer-limited? *Biophys. J. 79*, 992–1007.
39. Fromme, P., Jordan, P., and Krauss, N. (2001) Structure of photosystem I. *Biochim. Biophys. Acta 1507*, 5–31.
40. Nield, J., Morris, E. P., Bibby, T. S., and Barber, J. (2003) Structural analysis of the photosystem I supercomplex of cyanobacteria induced by iron deficiency. *Biochemistry 42*, 3180–3188.
41. Barber, J., Nield, J., Duncan, J., and Bibby, T. S. (2006) in Photosystem I: The light-driven plastocyanin:ferredoxin oxidoreductase, pp 99−117, Springer, Dordrecht, The Netherlands.
42. Melkozernov, A. N., Barber, J., and Blankenship, R. E. (2006) Light harvesting in photosystem I supercomplexes. *Biochemistry 45*, 331–345.
43. Kouřil, R., Yeremenko, N., D'Haene, S., Yakushevska, A. E., Keegstra, W., Matthijs, H. C., Dekker, J. P., and Boekema, E. J. (2003) Photosystem I trimers from *Synechocystis* PCC 6803 lacking the PsaF and PsaJ subunits bind an IsiA ring of 17 units. *Biochim. Biophys. Acta 1607*, 1–4.
44. Yeremenko, N., Kouřil, R., Ihalainen, J. A., D'Haene, S., van Oosterwijk, N., Andrizhiyevskaya, E. G., Keegstra, W., Dekker, H. L., Hagemann, M., Boekema, E. J., Matthijs, H. C., and Dekker, J. P. (2004) Supramolecular organization and dual function of the IsiA chlorophyll-binding protein in cyanobacteria. *Biochemistry 43*, 10308–10313.
45. Kouřil, R., Yeremenko, N., D'Haene, S., Oostergetel, G. T., Matthijs, H. C., Dekker, J. P., and Boekema, E. J. (2005) Supercomplexes of IsiA and photosystem I in a mutant lacking subunit PsaL. *Biochim. Biophys. Acta 1706*, 262–266.
46. Kouřil, R., Arteni, A. A., Lax, J., Yeremenko, N., D'Haene, S., Rogner, M., Matthijs, H. C., Dekker, J. P., and Boekema, E. J. (2005) Structure and functional role of supercomplexes of IsiA and Photosystem I in cyanobacterial photosynthesis. *FEBS Lett. 579*, 3253–3257.
47. Havaux, M., Guedeney, G., Hagemann, M., Yeremenko, N., Matthijs, H. C. P., and Jeanjean, R. (2005) The chlorophyll-binding protein IsiA is inducible by high light and protects the cyanobacterium *Synechocystis* PCC6803 from photooxidative stress. *FEBS Lett. 579*, 2289–2293.
48. Ardelean, I., Matthijs, H. C., Havaux, M., Joset, F., and Jeanjean, R. (2002) Unexpected changes in photosystem I function in a cytochrome

c6-deficient mutant of the cyanobacterium *Synechocystis* PCC 6803. *FEMS Microbiol. Lett. 213*, 113–119.
49. Jeanjean, R., Zuther, E., Yeremenko, N., Havaux, M., Matthijs, H. C., and Hagemann, M. (2003) A photosystem 1 psaFJ-null mutant of the cyanobacterium *Synechocystis* PCC 6803 expresses the isiAB operon under iron replete conditions. *FEBS Lett. 549*, 52–56.
50. Singh, A., McIntyre, L., and Sherman, L. (2003) Microarray analysis of the genome-wide response to iron deficiency and iron reconstitution in the cyanobacterium *Synechocystis sp.* PCC 6803. *Plant Physiol. 132*, 1825.
51. Anbar, A. D., and Knoll, A. H. (2002) Proterozoic ocean chemistry and evolution: A bioinorganic bridge? *Science 297*, 1137–1142.
52. Dupont, C. L., Yang, S., Palenik, B., and Bourne, P. E. (2006) Modern proteomes contain putative imprints of ancient shifts in trace metal geochemistry. *Proc. Natl. Acad. Sci. U.S.A. 103*, 17822–17827.
53. Holland, H. D. (2006) The oxygenation of the atmosphere and oceans. *Philos. Trans. R. Soc. London, Ser. B 361*, 903–915.
54. Bibby, T. S., Zhang, Y., and Chen, M. (2009) Biogeography of photosynthetic light-harvesting genes in marine phytoplankton. *PLoS One 4*, No. e4601.
55. Scanlan, D. J., Ostrowski, M., Mazard, S., Dufresne, A., Garczarek, L., Hess, W. R., Post, A. F., Hagemann, M., Paulsen, I., and Partensky, F. (2009) Ecological genomics of marine picocyanobacteria. *Microbiol. Mol. Biol. Rev. 73*, 249–299.
56. Bibby, T. S., Mary, I., Nield, J., Partensky, F., and Barber, J. (2003) Low-light-adapted *Prochlorococcus* species possess specific antennae for each photosystem. *Nature 424*, 1051–1054.
57. Chappell, P. D., and Webb, E. A. (2010) A molecular assessment of the iron stress response in the two phylogenetic clades of *Trichodesmium*. *Environ. Microbiol. 12*, 13–27.
58. Bowie, A. R. (1997) Biogeochemistry of Fe and other trace elements (Al, Co, Ni) in the upper Atlantic Ocean. *Deep-Sea Res., Part I 49*, 605–636.
59. Gao, Y., Kaufman, Y., Tanre, D., Kolber, D., and Falkowski, P. (2001) Seasonal distributions of aeolian iron fluxes to the global ocean. *Geophys. Res. Lett. 28*, 29–32.
60. Berman-Frank, I., Cullen, J., Shaked, Y., Sherrell, R., and Falkowski, P. (2001) Iron availability, cellular iron quotas, and nitrogen fixation in *Trichodesmium*. *Limnol. Oceanogr. 46*, 1249–1260.

Supporting Information

1. Supplementary Figures

Supplementary Figure S1: Overview schematic

When *T. elongatus* is grown at ecologically-relevant nM concentrations of Fe, the light-harvesting capacity of Photosystem I is increased nearly threefold relative to PSI complexes formed under Fe-replete conditions. This change in the cell's photosynthetic machinery can be linked to dramatic changes in the availability of Fe during the evolutionary history of the Cyanobacteria. By relating photosynthetic structures to environmental conditions, we can find traces of Earth's geochemical past in modern biochemistry.

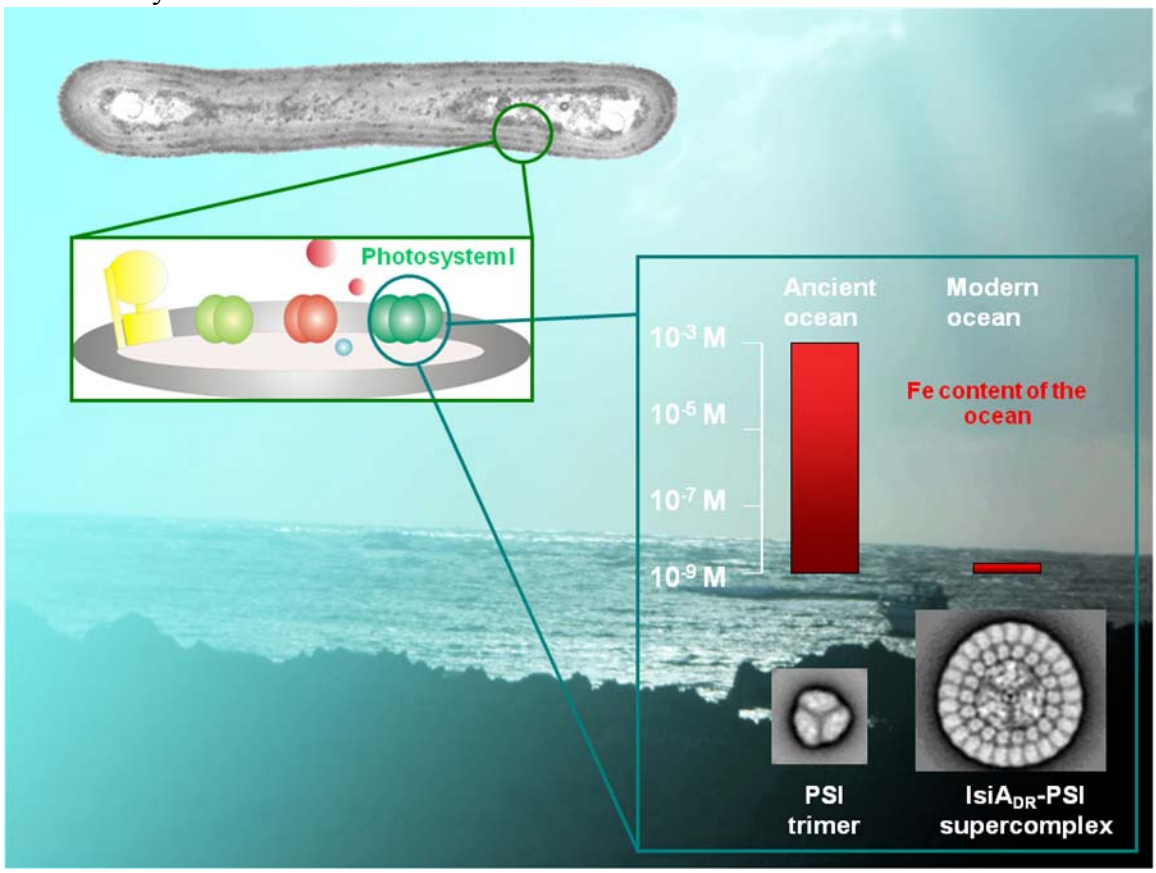

Supplementary Figure S2: Isolation of the of PSI-IsiA supercomplexes by ion exchange and size-exclusion chromatography

Anion exchange (a) and subsequent size exclusion elution profiles (b-e) for purification of various PSI-IsiA supercomplexes.
(a) The upper profile shows the separation of PSI-$IsiA_{SR}$ **(**single ring, first peak) and a mixture of PSI-$IsiA_{DR}$ and PSI-$IsiA_{PDR}$ supercomplexes (double and partially-formed double rings, second peak). The lower conductivity profile shows the required concentrations of $MgSO_4$. PSI-$IsiA_{SR}$ supercomplexes were further purified with a single round of gel filtration (b), while two rounds (c & d, e) were required to separate the PSI-$IsiA_{DR}$ supercomplex (d) from a population of PSI-$IsiA_{PDR}$ supercomplexes (e).

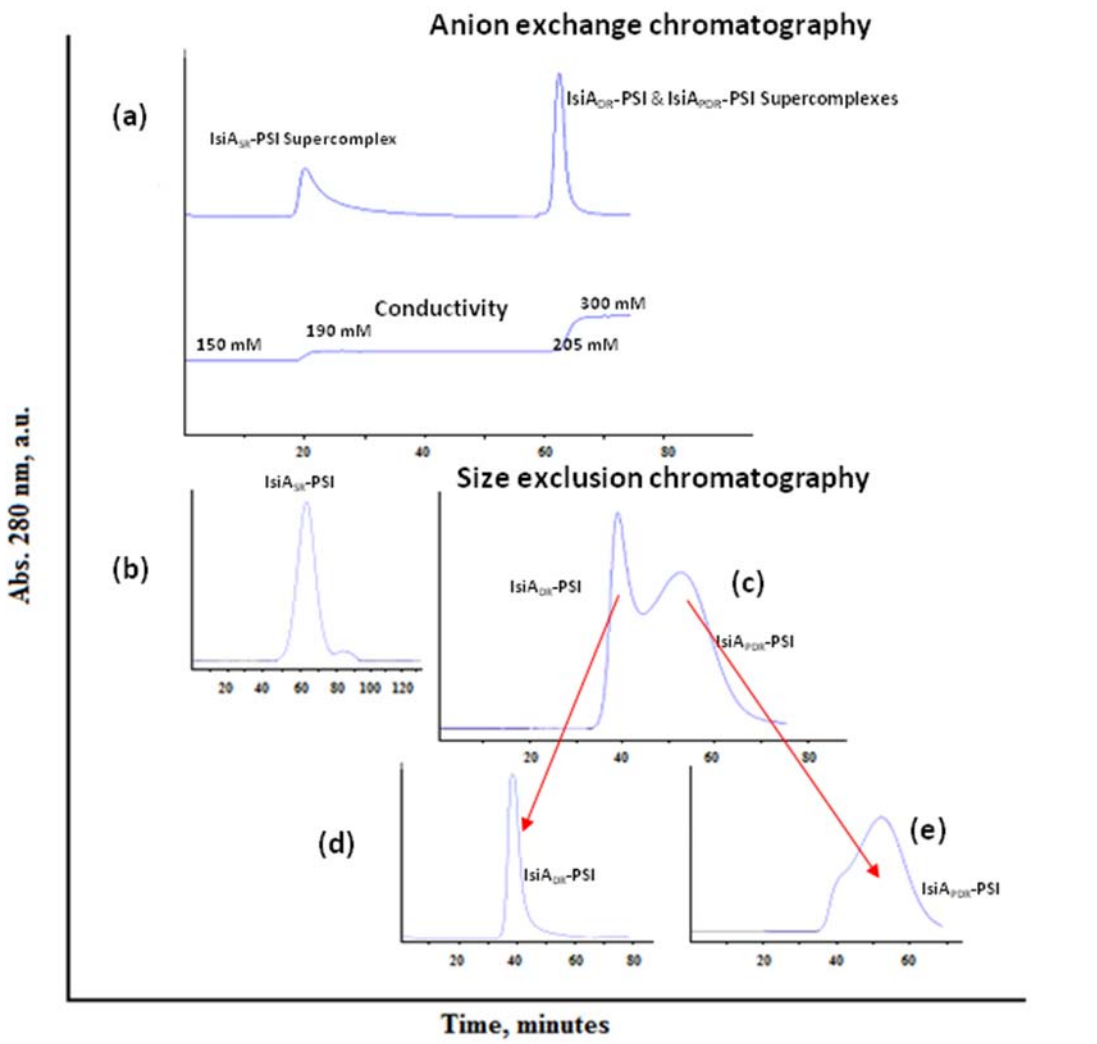

Supplementary Figure S3: SDS gel electrophoresis of the PSI-IsiA supercomplexes

SDS-PAGE of PSI trimer and different PSI-IsiA supercomplexes, purified by FPLC, showing the presence of IsiA in all the PSI-IsiA supercomplexes.
Lane 1: Complete double rings. (PSI-IsiA$_{DR}$)
Lane 2: Partial double rings. (PSI-IsiA$_{PDR}$)
Lane 3: Single ring. (PSI-IsiA$_{SR}$)
Lane 4: Dissolved PSI crystals. (PSI)
The gel was stained with silver

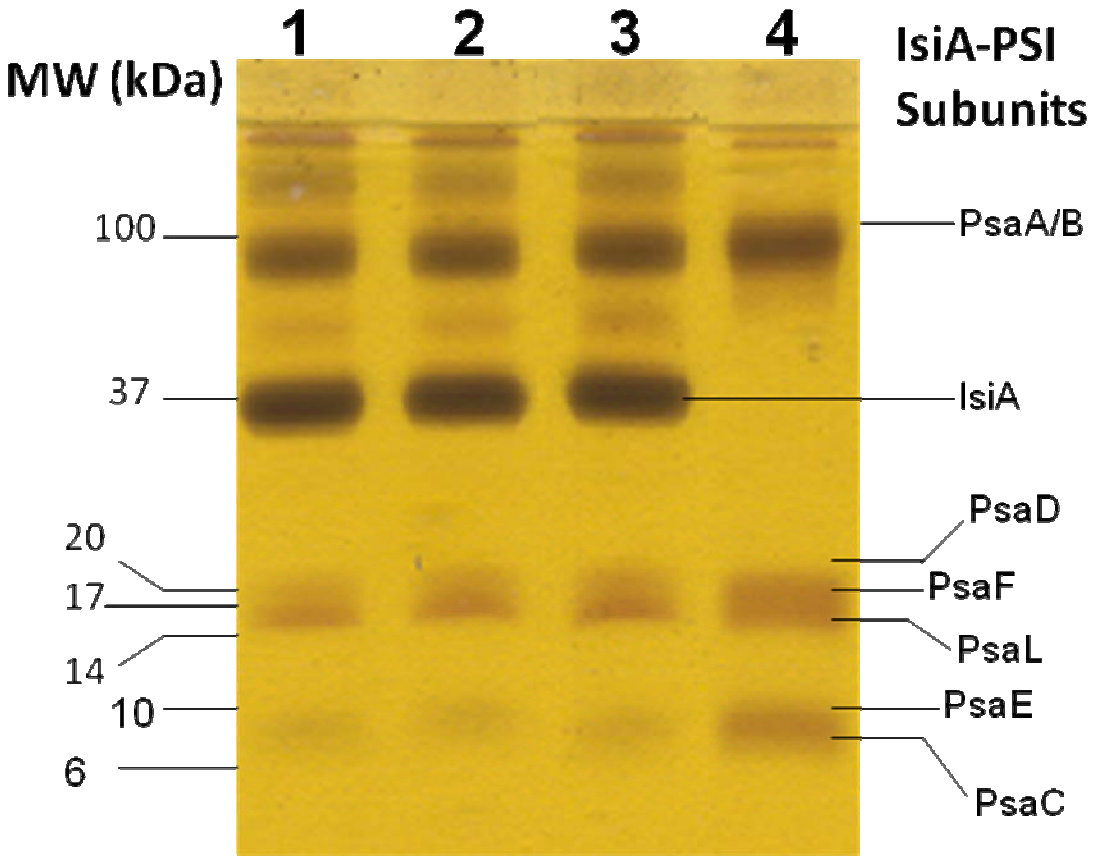

Supplementary Figure S4: Western blot showing the PsaC content of *T. elongatus* cells and the isolated PSI-IsiA$_{DR}$ complex

PsaC content of the different samples as determined by western blot with an antibody against PsaC (*Agrisera*). Equal amounts of P_{700} were loaded in lanes 1 and 2 and equal amounts of protein in lanes 3 and 4.

1- PSI-trimer
2- PSI-IsiA$_{DR}$ supercomplex
3- *T. elongatus* Whole cell extracts (Fe-replete conditions)
4- *T. elongatus* Whole cell extracts (nM Fe)
5- PsaC standard 0.225 pmol (cat#AS04 042S)
6- PsaC standard 0.45 pmol
7- PsaC standard 0.9 pmol

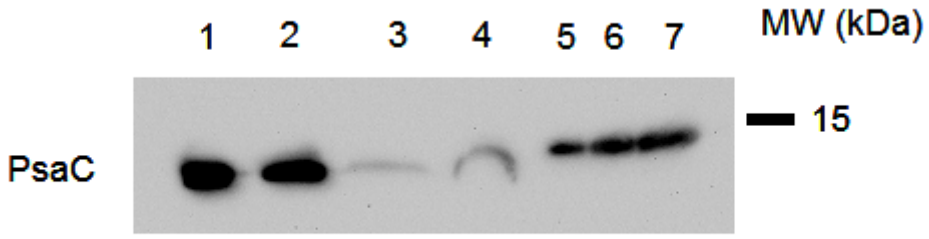

Supplementary Figure S5: P_{700}^{+} recombination kinetics

P_{700}^{+} recombination kinetics of PSI and the PSI-IsiA$_{DR}$ supercomplex at 700 nm.
The kinetics were determined as described in Materials and Methods.
(A) P_{700}^{+} reoxidation kinetics of PSI-trimers (*T. elongatus* wild type). Dissolved PSI crystals were used for this experiment.
(B) P_{700}^{+} reoxidation kinetics of PSI-IsiA$_{DR}$ supercomplexes isolated from cells that have been grown at 2.5 nM Fe.
The kinetics were very similar in both samples. The reoxidation of P_{700}^{+} was dominated by ms kinetics that are indicative of a back reaction with $(F_A/F_B)^{-}$, with kinetic constants of 46 ms for PSI (74.2%) and 82 ms for the PSI-IsiA$_{DR}$ supercomplexes (84.4 %). The discontinuity in the raw data at 20 ms was caused by the recording of the data in two separate channels.

(A)

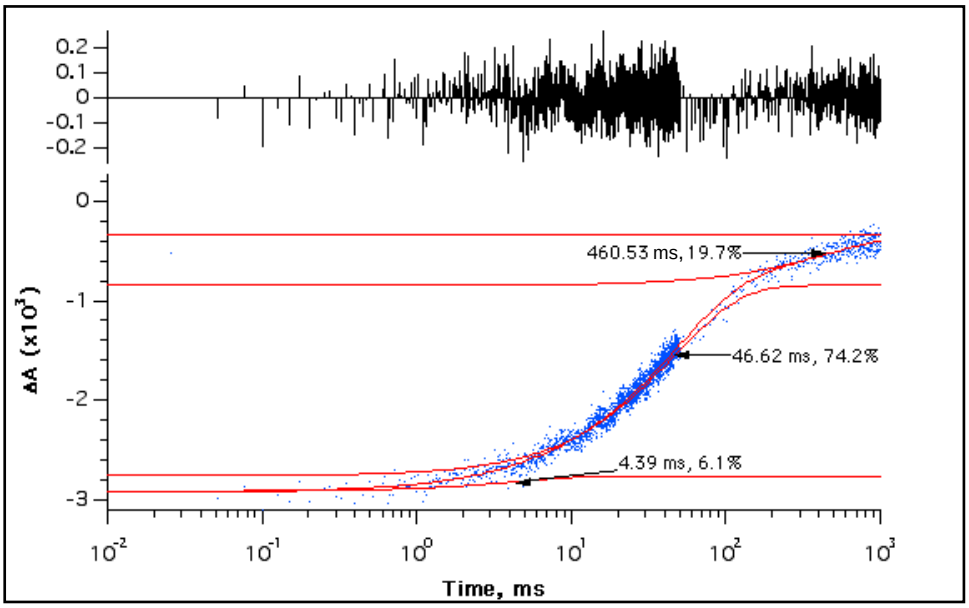

(B)

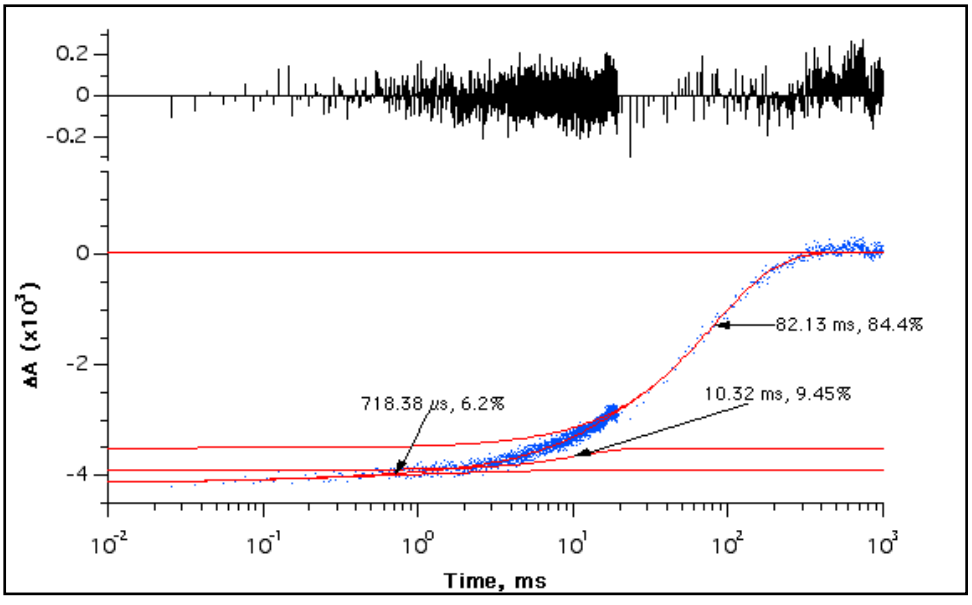

Supplementary Figure S6: FDAS of the PSI-IsiA supercomplexes from TCSPC

FDAS for various PSI-IsiA supercomplexes, as measured using time-correlated single photon counting. Although the spectral and temporal resolution of the TCSPC is lower than that obtained using the streak camera (see Fig. 2), the lifetimes and spectral shapes obtained are similar.

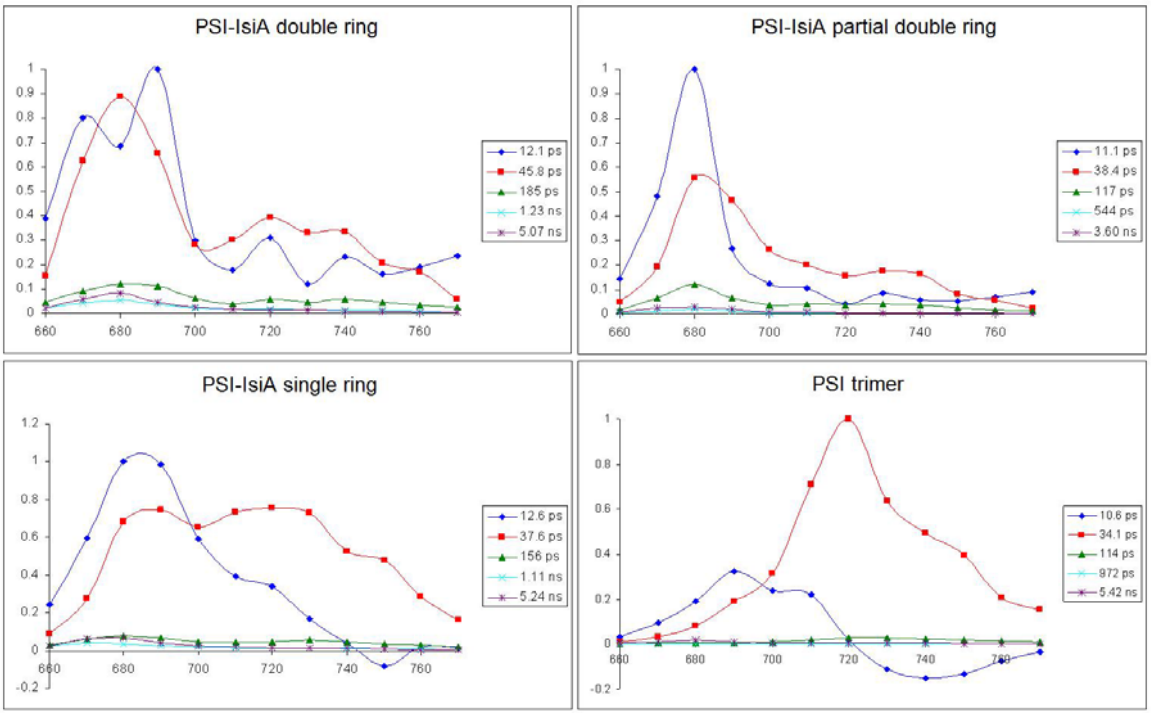

Supplementary Figure S7: FDAS at 10% excitation intensity

FDAS from streak camera measurement of the PSI-IsiA$_{DR}$ supercomplex at 10% of the normal excitation intensity. The agreement of lifetimes and spectral shapes with the full-intensity measurements suggests that the role of singlet-singlet annihilation in the excitation decay kinetics is negligible.

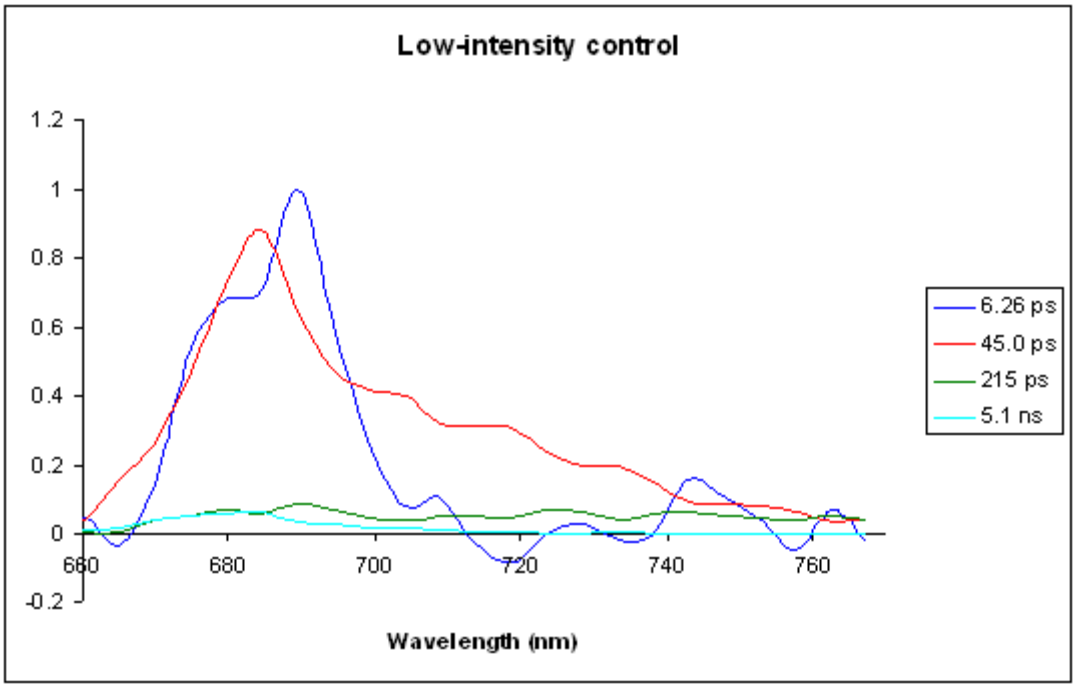

Supplementary Figure S8: Annotated TEM images showing protein-protein interactions

Images of the PSI-IsiA$_{DR}$ supercomplex (left) and a filtered 15 Å map of the PSI trimer reconstructed from the crystal structure show differences at the monomer-monomer interaction site (yellow box) as well as the flavodoxin docking site (cyan circle). The location of the PsaK subunit, which is important for monomer-monomer interactions, is indicated with a red arrow.

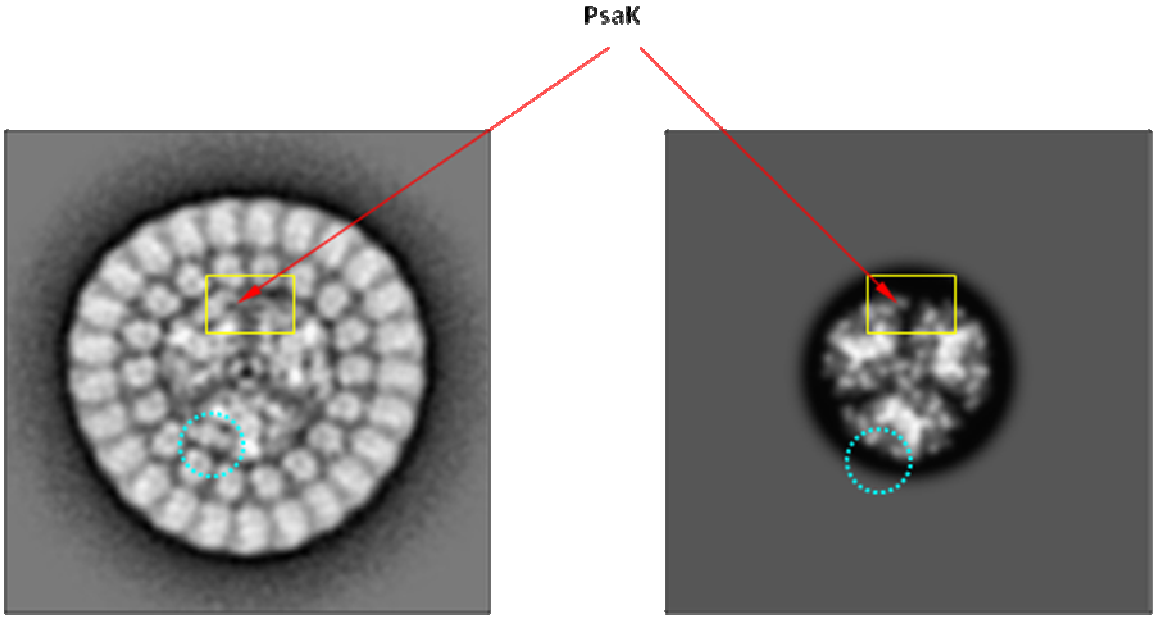

Supplementary Figure S9: Original transmission electron micrograph.

The images shown in Figure 1 were derived from 70,000 single-particle projections taken from 1,500 images like the one shown below. Note the presence of several complete PSI-IsiA$_{DR}$ supercomplexes as well as a few partial double rings in this micrograph. Scale bar is 100 nm.

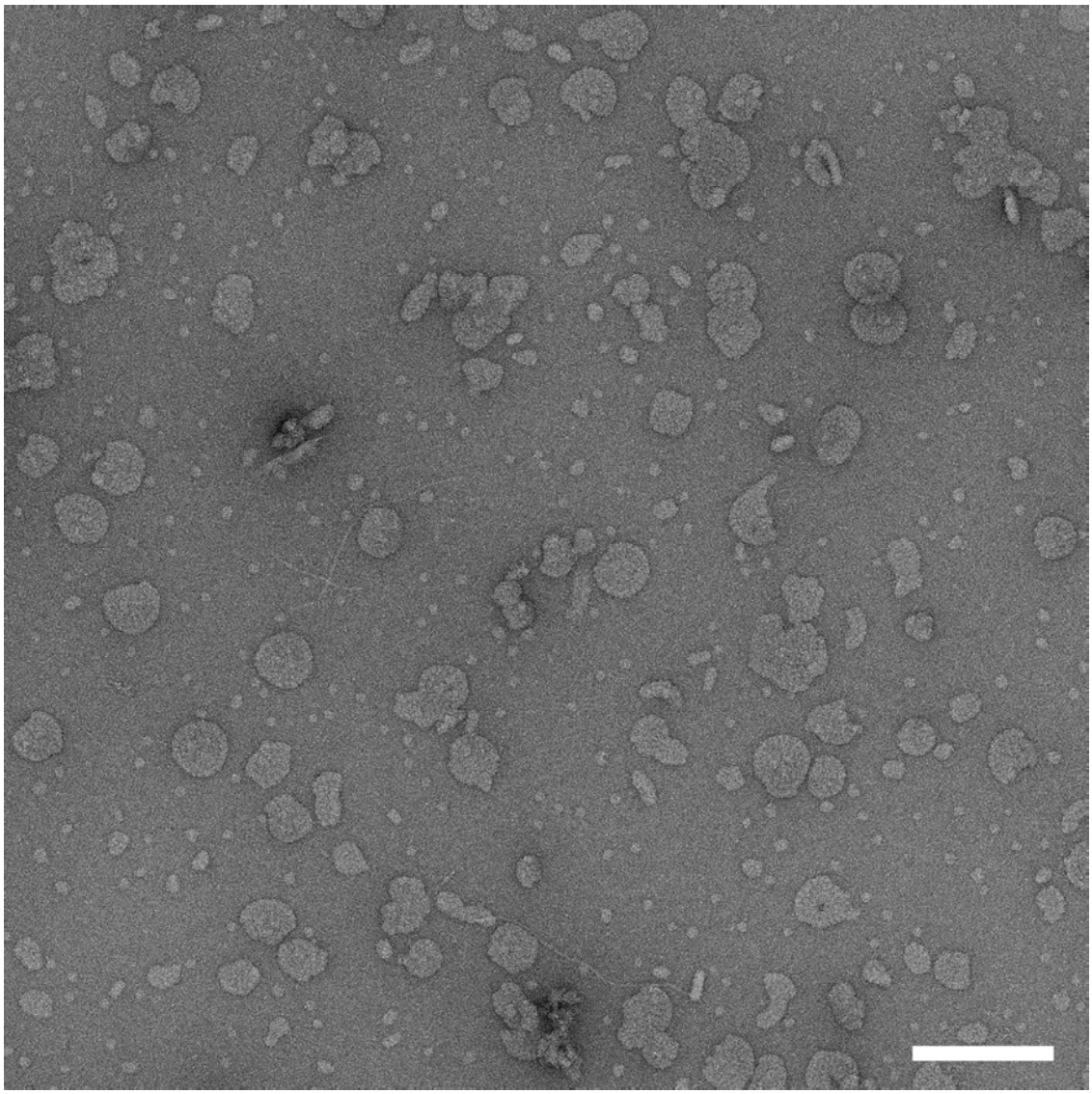

2. Supplementary Methods

Laser-flash induced absorption spectroscopy: Charge recombination kinetics from $(F_A/F_B)^-$ to P_{700}^+ were measured by monitoring the flash-induced absorbance change at 700 nm. The sample contained PSI-IsiA$_{DR}$ supercomplexes at a concentration of 45 μM chlorophyll in 50 mM MOPS pH 7.0, 0.04% β-DDM, 10 mM $MgCl_2$, 10 mM NaCl, 10 mM sodium ascorbate and 10 μM dichlorophenolindophenol. The sample was placed in a 1×1 cm (2.5 ml volume) quartz cuvette. As a control, the reoxidation kinetics of the PSI trimer (obtained from dissolved PSI crystals) were measured under identical conditions. Actinic illumination was provided by a Nd:YAG laser (Quanta-Ray DCR-11, *Spectra-Physics, Mountain View, CA*) operated in the second harmonic (532 nm) with a 7 ns duration and an energy of 2 mJ/cm^2. The measuring beam was derived from a 400 W tungsten-halogen lamp (model 66057, *Oriel Corp., Stratford, CT*), which was passed sequentially through a 1/4 m monochromator (Model 82-410, *Jarrel-Ash. Co., Waltham, MA)* and a shutter (*Uniblitz* model T132, *Vincent Associates, Rochester, NY*). The beam was monitored using a reverse-biased Si photodiode (PIN10D, UDT *Sensors, Inc., Hawthorne, CA*), which was shielded from stray light with a narrow-band interference filter centred at 700 nm (*Corion*). The shutter was opened 3 ms before the onset of the laser flash. The signal from the photodiode was amplified with a TM502A differential amplifier (Tektronix, Beaverton, OR), digitized with a DSA601 digital oscilloscope (*Tektronix*), and processed on a Macintosh computer (Model 9500, *Apple, Cupertino, CA*) that was interfaced with the digitizer via an IEEE-488 bus (*PCI-GPIB, National Instruments, Austin, TX*). The electronic bandwidth of the detection system was 1 MHz. Typically, 6 to 12 transients were averaged. Kinetic traces were analyzed by fitting the multi-exponential decay using the Marquardt least-squares algorithm program in Igor-Pro (*Wavemetrics, Lake Oswego*, *OR*).

Immunoblot analysis: Sample protein concentration was quantified using a fluorescent method (R33200; *Invitrogen*). Samples were then run on 12%, 15%, or 18% (w/v) polyacrylamide gels and then blotted onto polyvinylidene fluoridemembrane. The blots were then probed with anti-PsaC (AS04-042, *Agrisera, Inc.*). A horseradish peroxidase-conjugated secondary antibody (172–1019; *Bio-Rad Laboratories*) was used according to instructions and the blots were visualized with a chemiluminescent substrate system (34080; *Pierce Biotechnology*) and the blots were imaged using a CCD imager.

3. Supplementary Discussion

Cell growth: *Thermosynechococcus elongatus* was grown photoautotrophically under Fe-free conditions for 11 days to deplete the intracellular iron storage in the cells. On day 1, 2.5 nM Fe was added to the growth medium. It should be noticed that the culture remained dark green without any sign of chlorosis during the complete growth cycle and also no phycobillisome accumulation was observed after supplementation of the growth medium with nM iron. At the onset of Fe deficiency, a large number of PSI trimers with single rings are formed in the membrane. Within 3 to 4 weeks of adding nM Fe, the PSI-IsiA$_{SR}$ supercomplex (SR- single ring, 18 IsiA) was further surrounded by a full second

ring of IsiA proteins, forming a stable double ring structure. The number of PSI-IsiA$_{DR}$ supercomplexes increased with time. Nanomolar Fe conditions were tolerated very well and the fast cell growth under these conditions indicated that the cells did not suffer from decreased physiological activity. After 30 days, the cells were harvested and PSI-IsiA$_{DR}$ supercomplexes were purified from the thylakoids by ion exchange chromatography and two subsequent size exclusion chromatography steps (Fig. S2, Table S1).

Chl/P$_{700}$ ratio determination: The oxidized-minus-reduced difference spectrum of P$_{700}$ in the PSI-IsiA$_{DR}$ supercomplex was measured in a dual beam spectrophotometer to determine the ratio of Chl to P$_{700}$ (Table S1). For comparison, the spectra of dissolved crystals of trimeric PSI were analyzed using the same setup. The Chl/P$_{700}$ content of the PSI trimer was found to be 95 ± 1 Chl/P$_{700}$, which is in very good agreement with the X-ray crystal structure of the PSI complex, which shows 96 Chl/P$_{700}$ (*1*). If we assume that one IsiA protein contains 13 chlorophyll molecules (*2*) this would imply a total of 559 Chl can be bound to 43 IsiA proteins If we further assume 43 IsiA proteins/PSI trimer plus 3 x 96 Chl for the PSI core, this adds up to 847 Chl/PSI trimer, or 282 Chl/P$_{700}$, which is in very good agreement with the measurement.

Protein composition analysis: We have also studied the response of this cyanobacterium to complete and prolonged iron depletion. Under these conditions, cells undergo chlorosis and most of complexes were found to lack the stromal subunits (PsaC, PsaD and PsaE). This is consistent with full-genome microarray studies of *Synechocystis* sp. PCC 6803 under iron-stress conditions, which showed a decrease of more than 50% in the level of the *psaC* transcript (*3*). To determine whether the PSI-IsiA$_{DR}$ supercomplex contains the stromal subunits and the complete electron transport chain including the terminal iron-sulfur clusters, we analyzed the protein composition of the supercomplex (Fig. S3). The results of SDS gel electrophoresis show that the PSI-IsiA$_{DR}$ supercomplex grown under these conditions *does* contain PsaC, PsaD and PsaE, however quantification from silver-stained SDS gels is difficult. The PsaC content was therefore quantified by immunoblotting with antibodies against PsaC (Fig. S4). The results show that the PsaC content of the PSI-IsiA$_{DR}$ supercomplex is similar to that of PSI trimers and the PSI-IsiA$_{SR}$ supercomplex. Therefore, the reduction in PsaC content noted earlier is not directly correlated with the formation of PSI supercomplexes, and is only induced under severe Fe depletion conditions.

Laser Flash Spectroscopy: To ensure that the PsaC subunit still contains the terminal Fe$_4$S$_4$ clusters F$_A$ and F$_B$, we further analyzed the electron transport chain in the PSI-IsiA$_{DR}$ supercomplexes using time-resolved optical spectroscopy at 700 nm. Following a laser flash, each of the electron acceptors in PSI recombines with P$_{700}^+$ with a characteristic lifetime. If PsaC is present, the reduced Fe$_4$S$_4$ clusters will recombine with P$_{700}^+$ with a lifetime of ca. 100 ms; however, if PsaC is absent, the recombination time will be 1 ms if the terminal acceptor is F$_X$ or 10 to 100 µs if the terminal acceptor is A$_1$ (*4*). PSI trimers show a rapid bleaching followed by a charge recombination consisting of three kinetic phases. The most prominent phase, which accounts for 70% of the absorbance change, has a lifetime of ~50 ms, and is ascribed to the P$_{700}^+$ [F$_A$/F$_B$]$^-$ back reaction. The slowest kinetic phase, which accounts for 20% of the absorbance change, is

probably due to forward electron donation from Cyt c_6 when the [F_A/F_B] clusters have donated their electron to di-oxygen. The fastest kinetic phase, with a lifetime of ca. 4 ms, is likely due to the P_{700}^+ [F_X]$^-$ back reaction in PSI trimers that have lost PsaC (Fig. S5*A*). The PSI-IsiA$_{DR}$ supercomplexes show similar results (Fig. S5*B*); the most prominent phase, which accounts for 82% of the absorbance change, has a lifetime of ~80 ms, and is similarly ascribed to the P_{700}^+ [F_A/F_B]$^-$ back-reaction. The two faster phases are similarly ascribed to earlier acceptors that function in the absence of a small amount of PsaC. This indicates that the PSI-IsiA$_{DR}$ supercomplex incorporates an intact acceptor site with F_A and F_B present and functional in electron transfer.

Non-heme iron quantification: This conclusion was supported by analysis of non-heme iron in the two preparations. The iron content of the PSI trimer was determined by inductively-coupled plasma mass spectrometry (ICP-MS) to be 13.8 ± 2 Fe/P_{700} and the iron content of the PSI-IsiA$_{DR}$ supercomplex was determined to be 12.1 ± 2 Fe/P_{700}. Because 12 Fe/P_{700} are expected if PSI contains the three Fe_4-S_4 clusters F_X, F_B and F_A, PSI in the PSI-IsiA$_{DR}$ supercomplexes contains the complete complement of electron acceptors.

Single-particle electron microscopy: In EM images, the size and "resolution" of the IsiA complexes differ significantly between the outer and inner ring. The IsiA monomers in the inner ring show much finer structural details than any of the IsiA proteins in the single ring PSI-IsiA$_{SR}$ supercomplexes that have been described earlier, while the proteins in the outer ring show less structural detail and also appear to be larger than the IsiA monomers in the inner ring. The outer-ring subunits are comparable in size and resolution to the IsiA subunits in reported electron micrographs of PSI-IsiA$_{SR}$ supercomplexes. We calculated that the area occupied by each IsiA monomer in outer ring to be ~8 nm^2 larger than in the inner ring. The major reason for the size difference may be the presence of the detergent shell around the outer rings, either because the detergent is being imaged directly or because it slightly destabilizes the outer ring. The increased resolution of the IsiA proteins in the inner ring likely indicates that the presence of the outer ring leads to better ordering in the inner ring, due to a greater number of stabilizing protein-protein contacts.

A comparison of EM images of an PSI-IsiA$_{DR}$ supercomplex (Fig. 1*A*) with the structure of a PSI trimer at 15 Å resolution (derived from the 2.5Å resolution X-ray structure) (Fig. 1*B*) shows the same major structural features. However, the PSI trimers in the supercomplexes show more detailed features at the periphery. PSI monomers interact with each other at the periphery at more than one point in the PSI-IsiA$_{DR}$ supercomplex, whereas in PSI they have fewer interactions at the periphery where subunit PsaK is located (Fig. S8). PsaK is only loosely bound to the PSI trimer, which explains the partial disorder in the X-ray structure at 2.5 Å resolution (*1*). The extra density in the electron microscopic images of the PSI-IsiA$_{DR}$ supercomplex indicates that PsaK may be involved in the docking of IsiA subunits to PSI, assuming a more ordered conformation in the supercomplex.

The identification of assembly intermediates of supercomplexes that contain 16 and 19 subunits in an incomplete outer ring (Fig. 1*C*,*D*) indicates that the symmetry mismatch between the inner ring, which consists of 18 subunits, and the outer ring, which

consists of 25 subunits, is already established in the assembly phase of supercomplex formation. The detailed analysis of the position of the outer ring of IsiA proteins in the three different assembly intermediates indicates that the proteins are more densely packed in the complete double ring than in the assembly intermediates. This indicates that the IsiA protein must contain intrinsic flexible structural elements that allow both loose and tight packing. In this respect it is intriguing to note the increase in the structural order and resolution of the IsiA proteins of the inner ring upon binding the outer IsiA ring. It shows that despite its conserved interactions with PSI, IsiA has the ability to adjust its interactions according to structural requirements (Fig. 1C,D). This flexibility is another remarkable feature of PSI-IsiA$_{DR}$ supercomplexes. The PSI-IsiA$_{DR}$ supercomplex is the maximal auxiliary antenna system found for PSI trimers; we have not seen any supercomplexes with IsiA proteins in a third ring. In addition, no assembly intermediates other than the two depicted in Fig. 1 were observed at high enough frequencies to allow for satisfactory image reconstruction.

A previous electron microscopic analysis showed that terminal electron acceptor flavodoxin docks to PSI close to the stromal subunits PsaC and PsaD at a stromal hump that is located on the surface of PsaA. In this study flavodoxin extends the outer boundary of the PSI trimer (*5*). When these images are compared with EM pictures of the PSI-IsiA$_{DR}$ supercomplex, one sees that flavodoxin docks in a position where part of the protein could interact with the IsiA ring (Fig. S8)

In the absence of the PsaL subunit, PSI trimers cannot be formed anymore, and if mutant cells without this subunit are grown without iron most of the IsiA accumulates in incomplete rings at the PsaFJ side of the complex (*6, 7*). It was found that growth of *Synechocystis* PCC 6803 in a medium without iron not only results in the formation of PSI-IsiA supercomplexes of various sizes, but prolonged iron deficiency also lead to "empty" IsiA rings without associated photosystem (*8, 9*). After prolonged growth in media without added iron, IsiA appeared to be the only spectroscopically measurable pigment-protein complex. A spectroscopic study on isolated IsiA aggregates revealed a characteristic fluorescence emission band peaking at 687 nm at 5 K and very short fluorescence lifetimes at room temperature (*10*), suggesting a very pronounced non-photochemical quenching, in line with the predicted second role of IsiA as photoprotector (*11*). It should be noted that these empty rings, formed in heavily chlorotic cells on their way to cell death, do not contain any more PSI or PSII and may represent a last "safety valve" for energy dissipation and storage for chlorophyll that arose from degradation of PSI and PSII .

Ultrafast fluorescence spectroscopy: Two major changes in the fluorescence decay data result from the addition of IsiA proteins to the PSI trimer (Fig. 2). The first is a change in the spectral shape of the fastest phase (7-10 ps). This appears to be indicative of a decrease in the fraction of red-shifted chlorophyll molecules in the PSI-IsiA$_{DR}$ supercomplex relative to the PSI trimer. The second change involves the second-fastest component (with lifetimes of 36-44 ps), which shows a spectral shift to the blue and a slight increase in lifetime.

Although an increase in trapping time would be expected in an enlarged light-harvesting antenna, the modest scale of the observed increase is startling. The antenna size increases threefold between the PSI trimer and the PSI-IsiA$_{DR}$ supercomplex, but the

lifetime of this trapping component increases only 16%. This appears to be a strong contradiction of the elegant theoretical work of Pearlstein (*12*), which predicted that trapping lifetime should scale linearly with antenna size. These predictions had not been rigorously testable in the past; early efforts by Fleming and coworkers (*13*), were hampered by severe damage of PSI complexes under harsh detergent treatments.

This apparent contradiction can be resolved by observing that the change from the bare PSI trimer to the PSI-IsiA$_{DR}$ supercomplex involves more than merely a scaling up of the antenna. Because the red-shifted pigments are associated exclusively with the PSI core (rather than IsiA), the larger antennas have a different spectral composition than the smaller ones. In particular, the 720 nm peak of the trapping component in the PSI trimer suggests a trapping process that is limited by transfer from the energetically localized red states to P_{700}, while the 690 nm peak of the trapping component in PSI-IsiA suggests a diffusion-limited trapping process, where most excitation resides on the bulk chlorophylls prior to trapping by P_{700}. Thus, while the lifetimes of the second component in these two samples are similar, they represent physically different processes and a comparison with Pearlstein's predictions (which account *only* for diffusion-limited trapping) is unwarranted. PSI-IsiA supercomplexes from *T. elongatus* therefore provide an ideal model system in which a crossover between diffusion limited and transfer-to-trap limited kinetics can be observed.

The absence of any high-amplitude components on the >50 ps scale (as have been observed in eukaryotic PSI-LHCI supercomplexes (*14, 15*)) indicates that there are no large chlorophyll pools that are poorly coupled to P_{700}; the entire light-harvesting system is tightly-coupled. In fact, the small increases in decay lifetimes described above indicate that even the largest PSI-IsiA supercomplexes form a pigment network that is as well-integrated as that of the PSI trimer. This is in agreement with previous spectroscopic studies of single ring PSI-Isi$_A$ complexes (*16, 17*).

Close consideration of the averaged TEM images presented in Fig. 1 indicates that this efficient coupling is probably the result of close packing of the pigments and not highly specific inter-subunit contacts. The inner IsiA ring consists of 18 subunits which make contact with a PSI trimer with C_3 symmetry – this means that the interaction between PSI and IsiA takes place in six distinct protein environments. It is possible that the protein-protein interactions between IsiA and the periphery of PSI have been optimized by evolution to provide efficient excitation transfer across this interface. The outer IsiA ring contains 25 subunits and therefore lacks a C_3 axis of symmetry. This means that every one of the outer subunits experiences a unique environment and makes protein-protein contacts that are slightly different from all of its neighbours. It is highly unlikely that each of these 25 contact surfaces has been separately optimized to allow for efficient energy transfer across the interface between the two rings.

A more likely explanation for this efficient coupling is suggested by theoretical studies of antenna optimality in PSI (*18, 19*). The consensus that has emerged from structure-based exciton network models of PSI is that only a few pigment orientations – specifically, those closest to P_{700} – are highly optimized. Despite the intricate and well-ordered chlorophyll arrangement seen in the crystal structure of Cyanobacterial PSI (*1*), it is likely that its efficiency arises primarily from the packing of numerous chlorophyll pigments into as small a volume as possible. The large Förster radius of chlorophyll *a* and its relatively long excitation lifetime ensure that any closely-packed assembly will be

reasonably well-coupled. An extremely well-defined arrangement of IsiA subunits in PSI-IsiA$_{DR}$ supercomplexes may therefore be unnecessary for efficient light harvesting. This observation has clear implications for the design of artificial light-harvesting systems – close packing of pigments is probably far more important than detailed control over their spatial arrangement.

6. Supplementary References

1. Jordan, P., Fromme, P., Witt, H. T., Klukas, O., Saenger, W., and Krauß, N. (2001) Three-dimensional structure of cyanobacterial photosystem I at 2.5 Å resolution, *Nature 411*, 909-917.
2. Loll, B., Kern, J., Saenger, W., Zouni, A., and Biesiadka, J. (2005) Towards complete cofactor arrangement in the 3.0 Å resolution structure of photosystem II, *Nature 438*, 1040-1044.
3. Singh, A., McIntyre, L., and Sherman, L. (2003) Microarray analysis of the genome-wide response to iron deficiency and iron reconstitution in the cyanobacterium *Synechocystis sp.* PCC 6803, *Plant Physiol. 132*, 1825.
4. Vassiliev, I. R., Jung, Y. S., Mamedov, M. D., Semenov, A., and Golbeck, J. H. (1997) Near-IR absorbance changes and electrogenic reactions in the microsecond-to-second time domain in Photosystem I, *Biophys. J. 72*, 301-315.
5. Mühlenhoff, U., Kruip, J., Bryant, D. A., Rögner, M., Sétif, P., and Boekema, E. (1996) Characterization of a redox-active cross-linked complex between cyanobacterial photosystem I and its physiological acceptor flavodoxin, *EMBO J. 15*, 488-497.
6. Aspinwall, C. L., Duncan, J., Bibby, T., Mullineaux, C. W., and Barber, J. (2004) The trimeric organisation of photosystem I is not necessary for the iron-stress induced CP43' protein to functionally associate with this reaction centre, *FEBS Lett 574*, 126-130.
7. Kouřil, R., Yeremenko, N., D'Haene, S., Oostergetel, G. T., Matthijs, H. C., Dekker, J. P., and Boekema, E. J. (2005) Supercomplexes of IsiA and photosystem I in a mutant lacking subunit PsaL, *Biochim Biophys Acta 1706*, 262-266.
8. Yeremenko, N., Kouřil, R., Ihalainen, J. A., D'Haene, S., van Oosterwijk, N., Andrizhiyevskaya, E. G., Keegstra, W., Dekker, H. L., Hagemann, M., Boekema, E. J., Matthijs, H. C., and Dekker, J. P. (2004) Supramolecular organization and dual function of the IsiA chlorophyll-binding protein in cyanobacteria, *Biochemistry 43*, 10308-10313.
9. Kouřil, R., Arteni, A. A., Lax, J., Yeremenko, N., D'Haene, S., Rogner, M., Matthijs, H. C., Dekker, J. P., and Boekema, E. J. (2005) Structure and functional role of supercomplexes of IsiA and Photosystem I in cyanobacterial photosynthesis, *FEBS Lett 579*, 3253-3257.
10. Ihalainen, J. A., D'Haene, S., Yeremenko, N., van Roon, H., Arteni, A. A., Boekema, E. J., van Grondelle, R., Matthijs, H. C., and Dekker, J. P. (2005) Aggregates of the chlorophyll-binding protein IsiA (CP43') dissipate energy in cyanobacteria, *Biochemistry 44*, 10846-10853.

11. Sandström, S., Park, Y. I., Oquist, G., and Gustafsson, P. (2001) CP43', the *isiA* gene product, functions as an excitation energy dissipator in the cyanobacterium *Synechococcus* sp PCC 7942, *Photochem. Photobiol. 74*, 431-437.
12. Pearlstein, R. M. (1982) Linear dependence of exciton lifetime on fractional absorbance of exciting light by reaction centers in photosynthetic units, *Biophys. J. 37*, A112-A112.
13. Owens, T. G., Webb, S. P., Mets, L., Alberte, R. S., and Fleming, G. R. (1987) Antenna size dependence of fluorescence decay in the core antenna of photosystem I: estimates of charge separation and energy transfer rates, *Proc. Natl. Acad. Sci. USA 84*, 1532-1536.
14. Melkozernov, A. N., Kargul, J., Lin, S., Barber, J., and Blankenship, R. E. (2004) Energy coupling in the PSI-LHCI supercomplex from the green alga *Chlamydomonas reinhardtii*, *J. Phys. Chem. B 108*, 10547-10555.
15. Ihalainen, J. A., Croce, R., Morosinotto, T., van Stokkum, I. H. M., Bassi, R., Dekker, J. P. X., and van Grondelle, R. (2005) Excitation decay pathways of Lhca proteins: A time-resolved fluorescence study, *J. Phys. Chem. B 109*, 21150-21158.
16. Melkozernov, A. N., Bibby, T. S., Lin, S., Barber, J., and Blankenship, R. E. (2003) Time-resolved absorption and emission show that the CP43' antenna ring of iron-stressed synechocystis sp. PCC6803 is efficiently coupled to the photosystem I reaction center core, *Biochem. 42*, 3893-3903.
17. Andrizhiyevskaya, E. G., Frolov, D., van Grondelle, R., and Dekker, J. P. (2004) Energy transfer and trapping in the Photosystem I complex of Synechococcus PCC 7942 and in its supercomplex with IsiA, *Biochim. Biophys. Acta-Bioenergetics 1656*, 104-113.
18. Şener, M. K., Lu, D. Y., Ritz, T., Park, S., Fromme, P., and Schulten, K. (2002) Robustness and optimality of light harvesting in cyanobacterial photosystem I, *J. Phys. Chem. B 106*, 7948-7960.
19. Vasil'ev, S., and Bruce, D. (2004) Optimization and evolution of light harvesting in photosynthesis: The role of antenna chlorophyll conserved between photosystem II and photosystem I, *Plant Cell 16*, 3059-3068.